




Cite this: *RSC Adv.*, 2024, 14, 15071

# A lost piece of the puzzle of the alkane cracking mechanism: a carbanion pathway on a solid base catalyst†

Zhixuan Zuo,<sup>‡</sup> Yuchen Sha,<sup>‡</sup> Ruoyu Wang,<sup>‡</sup>  Lixin Wang, Haitao Song, Peng Wang<sup>‡</sup> \* and Zhijian Da\*

The alkane cracking mechanism has been a subject of intense scrutiny, with carbonium and free radical mechanisms being two well-established pathways which correlate to solid acid catalysis and thermal cracking, respectively. However, despite an understanding of these two mechanisms, certain intricacies remain unexplored, especially when it comes to alternative reaction routes over solid base materials. This gap in the knowledge hinders optimization of the desired product selectivity of alkane cracking processes. In this work, solid superbases were first prepared by impregnation of NaNO<sub>3</sub> on MgO. The Na/MgO catalysts were characterized by XRD, BET, XPS and CO<sub>2</sub>-TPD techniques. To investigate the role of solid base materials, propane cracking was conducted over MgO and Na/MgO. SiO<sub>2</sub> was chosen as a representative of thermal cracking. Na/MgO showed better selectivity for light olefins than MgO or SiO<sub>2</sub>. Ethylene and light olefin selectivity could reach about 65.8% and 91.7%, respectively. Meanwhile, in terms of Na/MgO, the ratio of ethylene selectivity and propylene selectivity is greater than 2, exhibiting the advantage of selectivity for ethylene, which is obviously different from MgO and SiO<sub>2</sub>. Propane cracking over Na/MgO with different loading amounts of NaNO<sub>3</sub> was investigated further. The conversion rates of the samples presented a "volcano curve" with increasing Na content. Furthermore, DFT calculation showed that the base-catalyzed process of the propane cracking reaction follows a carbanion mechanism. The better product distribution and stronger surface base sites can be ascribed to charge transfer arising from the loading of NaNO<sub>3</sub>.

Received 3rd February 2024

Accepted 25th April 2024

DOI: 10.1039/d4ra00878b

rsc.li/rsc-advances

## 1. Introduction

Light olefins such as ethylene and propylene are important chemical building blocks, which are honored as the keystones of modern industry. The production capacity of ethylene and propylene is one of the most significant emblems of the economic strength and industrialization level of a country.<sup>1</sup> At present, there are various technologies for the production of light olefins, such as steam cracking, catalytic cracking, propane dehydrogenation, methanol to olefins, and ethanol to olefins, among which steam cracking has been the major route for the production of light olefins, accounting for more than 90% and 50% of the yield of ethylene and propylene, respectively.<sup>1–3</sup> However, the reaction temperature of steam cracking usually exceeds 800 °C, with higher CO<sub>2</sub> emission and less desired product distribution. In particular, ethane is

frequently used as feedstock in some new steam cracking units, where propylene is typically co-produced in a limited yield as a by-product with the production of ethylene.<sup>4,5</sup> Compared with the traditional steam cracking process for hydrocarbons, catalytic cracking offers a lower operating pressure and temperature. Moreover, investment in a catalytic cracking unit is lower as well.<sup>6–8</sup> Besides reducing the reaction temperature and energy consumption, the process is adaptable to a variety of feedstocks, and the product distribution can be flexibly regulated at the same time.<sup>9–12</sup> Zeolite, a typical solid acid material, is usually used as the most important component in a catalytic cracking catalyst. In the past several decades, numerous studies have proven that the hydrocarbon molecules are converted into light olefins in a carbonium ion mechanism over the zeolite catalyst. However, these catalysts are usually recognized to be sensitive to S, N, and heavy metals, *e.g.* Fe, Ni and V. In addition, coke formation on the zeolite *via* an excessive hydrogen transfer reaction over the acid site could also impede the cracking selectivity.<sup>13,14</sup>

Over the past several decades, a great deal of prior work has been focused on the development and application of acid catalysts in the catalytic cracking process, while the development of basic catalysts has been virtually ignored due to their

Sinopec Research Institute of Petroleum Processing Co., Ltd., No. 18 Xueyuan Road, Haidian District, Beijing, 100083, P. R. China. E-mail: wangpeng.ripp@sinopec.com; dazhijian.ripp@sinopec.com; Tel: +86-10-82368547; +86-10-82368390

† Electronic supplementary information (ESI) available. See DOI: <https://doi.org/10.1039/d4ra00878b>

‡ These three authors contribute equally to this work.



more complicated and expensive preparation process compared with that of solid acid catalysts, smaller specific surface area, poor structural strength, weak hydrothermal stability, and the fact that both CO<sub>2</sub> and H<sub>2</sub>O in the air are easily adsorbed on the active sites of the solid base, leading to passivation of the solid base.<sup>15–22</sup> Moreover, the reaction temperature, C/O (catalyst to oil) ratio and atmosphere could also have significant impacts on product selectivity. For instance, in terms of Li/MgO, the oxygen concentration had a considerable influence on hexane conversion and selectivity for products, especially CO<sub>x</sub>.<sup>23–26</sup>

In recent years, the hydrocarbon cracking process for light olefin production *via* base-catalysis has drawn much attention due to its general anti-coking performance and good stability of the solid base-catalysis compared to liquid base catalysis.<sup>27</sup> Solid base catalysts like N-Co/ $\gamma$ -Al<sub>2</sub>O<sub>3</sub> and Li/MgO were investigated for the production of light olefins *via* oxidative cracking of hydrocarbons. The conversion of *n*-butane of 82 wt% could be achieved by the utilization of N-Co/ $\gamma$ -Al<sub>2</sub>O<sub>3</sub> under an oxygen atmosphere at 600 °C, with the yields of ethylene and propylene reaching 31 wt% and 13 wt%, respectively.<sup>28</sup> Li/MgO prepared by the sol-gel method was shown to be a good catalyst with 28 mol% hexane conversion and 60 mol% light olefin selectivity at a lower reaction temperature of 575 °C.<sup>23</sup> KVO<sub>3</sub>/Al<sub>2</sub>O<sub>3</sub> prepared by impregnation was used as a catalyst in the catalytic pyrolysis reaction of naphtha, in which the KVO<sub>3</sub> component showed better anti-carbon-deposition ability. The yields of ethylene and propylene at a reaction temperature of 800 °C were increased by 10% and 5%, respectively, compared with thermal cracking.<sup>29</sup> Recently, calcium aluminate (CaAl) solid base catalysts were applied in the catalytic cracking of heavy oils. Niwamanya *et al.* presumed that the strong basicity of calcium aluminate could promote the dehydrogenation of hydrocarbon molecules, thereby raising the yield of light olefins, compared to silica sand.<sup>30</sup> In addition, Tian *et al.* further studied the performance of a calcium aluminate (CaAl) catalyst in catalytic cracking reactions. It was suggested that the catalyst promoted the generation of free radicals by hydrogen abstraction of the reactants and thus improved the yield of light olefins.<sup>31–34</sup> Recently, Wu *et al.* claimed a base-catalyzed technology named DPC (direct petroleum cut to chemicals and materials) for the catalytic cracking of heavy oil. It was proposed that the conversion of the heavy oil over the DPC base catalyst followed a carbanion reaction mechanism, but no evidence was provided to prove such a conjecture.<sup>35</sup> Moreover, the physical and chemical properties of the basic catalysts and the structure-activity relationships during the catalytic reaction were barely determined in the above cases, and the catalytic mechanism for the base-catalytic process has not been explained in detail.

Currently, many metal oxides and basic components have been used in the synthesis and studies of the catalytic performance of solid base catalysts, such as Al<sub>2</sub>O<sub>3</sub>, MgO and Na<sub>2</sub>O. Among them, Al<sub>2</sub>O<sub>3</sub> has been studied more due to its amphoteric properties, and the OH groups on its surface provide weakly basic sites with a Hammett index of <7.2.<sup>36</sup> Although most current Al<sub>2</sub>O<sub>3</sub>-based catalysts are valued for their acidic sites, the involvement of basic sites in the catalytic process is unavoidable.<sup>37</sup> Magnesium oxide is a typical solid base catalyst

and has been more widely and intensively studied among metal oxides due to its easier preparation by heat treatment and the easier availability of well-structured samples. The basic sites of magnesium oxide are usually considered to be defects in the lattice and lattice oxygen of magnesium oxide, and their basic strength varies with pretreatment conditions, with treatments at 450 °C in a vacuum giving basic strengths with Hammett indexes ranging from 18.4 to 26.5.<sup>38</sup> It has been found that the loading of Na species on MgO provides stronger base sites with Hammett indexes of 26.5–35.0, and this improvement has also attracted more attention.<sup>39</sup>

Herein, in order to investigate the mechanism of base-catalyzed cracking over solid base materials with different basic strengths, MgO, and a series of Na/MgO samples prepared by NaNO<sub>3</sub> impregnation with different loading amounts were prepared to represent regular solid base and solid superbase (base strength H<sub>+</sub> of at least +26), respectively. Then, propane, as a model compound due to its structural simplicity, was chosen to evaluate the differences in catalytic activity and selectivity of the above catalysts. In order to discriminate the difference between base-catalyzed and thermal cracking, an SiO<sub>2</sub> sample was investigated as well. Moreover, with the aim of gaining an insight into the catalytic mechanism of a base-catalyzed process, DFT calculation was further conducted to explain the catalytic performances of the base catalysts.

## 2. Experimental section

### 2.1 Catalyst preparation

**2.1.1 Silicon dioxide and magnesium oxide.** The silicon dioxide (Damao, AR) and commercial magnesium oxide used in this paper were provided by Tianjin Damao Chemical Reagent Factory and SINOPEC Catalyst Co. Ltd. Qilu Company, respectively. They were all processed by temperature-programmed calcination at 700 °C for 6 hours in the presence of air before use, and these two final samples were denoted “SiO<sub>2</sub>” and “MgO”.

**2.1.2 Sodium nitrate supported on magnesium oxide.** Samples of sodium nitrate supported on magnesium oxide were synthesized using an equal volume impregnation method. The commercial magnesium oxide was submerged in an aqueous solution of sodium nitrate (Sinopharm Chemical Reagent Co., Ltd, AR) with a calculated amount equivalent to 1, 5, 10, 15 wt% of sodium oxide, respectively. The sample was ultrasonically stood at room temperature for 4 hours and then dried in an oven at 120 °C overnight to remove excess water. The resultant material was finally treated with temperature-programmed calcination to 700 °C for 6 h in a muffle furnace in the presence of air and the samples were denoted “1-Na/MgO”, “5-Na/MgO”, “10-Na/MgO”, and “15-Na/MgO”.

### 2.2 Characterization

Several characterization techniques were used to investigate the properties of the samples examined in this article.

Elemental analysis of the prepared samples was carried out with X-ray fluorescence (XRF) using a 3271E X-ray fluorescence



spectrometer (Rigaku Corporation, Japan) with the following test conditions: Rh target, excitation voltage 54 kV, excitation current 50 mA.

X-ray diffraction (XRD) patterns were recorded on a D5005D XRD instrument (Siemens, Germany) with Cu K $\alpha$  radiation at 40 kV and 40 mA and a scanning speed of 10° min<sup>-1</sup> for shape and phase investigation.

The textural properties of the catalysts were determined on a Micromeritics ASAP 2420 instrument with the aid of nitrogen adsorption at 77 K after outgassing the samples for 4 h under 10<sup>-2</sup> Pa.

The pretreatment temperature required for the prepared samples and the effect of high-temperature calcination on the catalyst were determined by thermogravimetry-mass spectrometry (TG-MS). The TG-MS instrument performed simultaneously using a thermogravimeter (Labsys Evo STA, France) and a quadrupole mass spectrometer (Pfeiffer Vacuum QMS 422, France) and the signals were recorded for *m/z* 32, 44, and 30, which were considered to be molecular weight ions of O<sub>2</sub>, CO<sub>2</sub>, and NO, respectively.

The base property of the catalysts was determined by CO<sub>2</sub>-temperature-programmed desorption (CO<sub>2</sub>-TPD) technique of CO<sub>2</sub>-preadsorption using an Autochem II 2950 unit equipped with a thermal conductivity detector. Typically, a sample of 300 mg was thermally treated in the presence of helium gas at 850 °C for 2 h, and then the temperature of the sample was cooled to 100 °C and subsequently the gas flow was switched from helium to CO<sub>2</sub>/He gas (10 vol% CO<sub>2</sub>, 50 mL min<sup>-1</sup>) for 30 min. Then the sample was flushed with helium gas for 1 h to remove the physically adsorbed CO<sub>2</sub> molecules. Finally, the responses from the thermal conductivity detector were recorded at a ramp of 10 °C min<sup>-1</sup> from 100 °C to 850 °C under helium gas flow to obtain the CO<sub>2</sub>-TPD patterns of the samples.

The crystal size, morphology, and microanalysis of the elements (EDS-mapping) were examined with a HITACHI S-4800 scanning electron microscope (SEM).

The basic strength of the samples was determined by the Hammett index method, whereby the basic catalysts were measured by probe molecules with specific acidic strengths, and the basic strength was evaluated by a color reaction. H<sub>-</sub> is the base strength determined from the pK<sub>a</sub> value of an adsorbed indicator according to H<sub>-</sub> = pK<sub>a</sub> + log(B<sup>-</sup>)/(BH), where pK<sub>a</sub> is the negative logarithm of the dissociation constant of the indicator, BH is the concentration of the acidic form of the indicator, and B<sup>-</sup> is the concentration of the basic form. The (B<sup>-</sup>)/(BH) ratio is considered to be 1. In this experiment, bromothymol blue, 4-chloro-2-nitroaniline, 4-nitroaniline, 4-chloroaniline, and diphenylmethane were used as indicators for measuring basicity, and the specific color-changing reactions, data, and information about the indicators are listed in Table S1.† First, a calculated amount of the indicator was placed in a small glass vial and a calculated amount of fully dehydrated pure benzene was added to formulate a 1% solution of the indicator, which was closed completely with a seal to avoid the effects of carbon dioxide and water in the air. Another clean vial was taken and 2 mL of completely dehydrated pure benzene liquid was added; 0.1 g of solid base catalyst powder that had been roasted and

dried in preparation was weighed and added to the vial, which was quickly and completely sealed with a sealing sticker and lightly shaken. An appropriate amount of indicator solution was extracted with a syringe and added into the above vials, and left for 12 h for observation. When one vial shows acid color and the other vial shows base color, the base strength of the solid base catalyst will be between the two values.

### 2.3 Evaluation of catalytic performance

The evaluation method used was pyrolysis gas chromatography (PY-GC) which can make the feedstock vaporize and react with the catalysts quickly; the products directly enter the gas chromatography analysis system for separation and analysis. Catalytic cracking of propane over the prepared samples was carried out in a multi-functional pyrolysis analysis system, which consisted of a gas chromatograph (Agilent 8890, United States) and a single micro-furnace rapid reactor (Frontier Lab Rx-3050SR, Japan) fitted directly onto the aforementioned gas chromatograph. The catalysts were initially pressed, crushed, and sorted into grains of 40 to 60 mesh before the experiment. A sample of 0.1 g was loaded into a quartz reaction tube and fixed at both ends with porous quartz paper. The device was connected after placing the quartz reaction tube into the reactor and then pretreated *in situ* at 500 °C for 1 h in the reactor mentioned above. Subsequently, the propane gas (≥99%) quantified at 0.25 mL through a quantitative loop was passed through the reactor to interact with 0.1 g of catalyst at a desired temperature. The cracking products were carried by the carrier gas (high-purity nitrogen) directly into the vaporization chamber of the gas chromatograph through a specially made connecting needle under the micro-furnace reactor, and then into the gas chromatographic analysis system equipped with FID and TCD detectors for on-line qualitative and quantitative analysis of the products. A more detailed scheme of the experimental device for catalytic performance testing of the catalysts is shown in Fig. S1.† Eventually, the areas of all product peaks were summed to obtain the total absolute peak area (TAPA). The relative content of each component was calculated according to the area-normalization method. Thus, the conversion of propane and the selectivity of the products were calculated according to the following equations.

$$X_{\text{propane}} = \frac{\text{Peak area of propane}}{\text{TAPA}} \times 100\%$$

$$\text{Selectivity}_{\text{C}_x\text{H}_y} = \frac{\text{Peak area of C}_x\text{H}_y}{\text{TAPA} - \text{Peak area of C}_x\text{H}_y} \times 100\%$$

### 2.4 Computational details

Density functional theory (DFT) calculations were performed using Materials Studio 8.0 from BIOVIA. The optimizations performed on the compounds and the search for reactive transition states were carried out mainly using the Dmol<sup>3</sup> model. The functional was M06-L, DNP base cluster. The inner



electrons were processed using the all-electron approach. After optimization on the structures of the reactants and products, the transition states for each elementary reaction were searched with the LST/QST method. The adaptive convergence thresholds for energy, gradient and shift amounted to  $1.0 \times 10^{-5}$  Ha,  $0.002 \text{ Ha} \cdot \text{\AA}^{-1}$  and  $0.005 \text{ nm}$ , respectively. The surface adsorption energy ( $\Delta E_{\text{ads}}$ ) was calculated with the following equation:  $\Delta E_{\text{ads}} = E_{\text{surface-sub}} - E_{\text{surface}} - E_{\text{sub}}$ , where  $E_{\text{surface-sub}}$ ,  $E_{\text{surface}}$ , and  $E_{\text{sub}}$  are the adsorption energy of propane in the substrate, the energy of the bare substrate, and the energy of the adsorbate, respectively.

## 3. Results and discussion

### 3.1 Textural characterization of the catalysts

The powder X-ray diffraction patterns of bare MgO and sodium-nitrate-modified MgO are shown in Fig. 1. The major diffraction peaks at  $2\theta = 36.9^\circ$ ,  $42.9^\circ$ , and  $62.3^\circ$  in both MgO and 5-Na/MgO samples can be assigned to the (1,1,1), (2,0,0), and (2,2,0) facets of MgO in the periclase crystalline phase. Both the peak positions and the peak widths at half height are almost identical, indicating that the structure of MgO remained intact during the preparation of the 5-Na/MgO catalyst. By comparing the XRD patterns of the MgO and 5-Na/MgO samples, it is found that the intensity of the diffraction peaks corresponding to MgO decreases slightly, indicating that the introduction of Na only decreases the content of MgO. The appearance of new diffraction peaks indicates the introduction of new crystal phases. The smaller diffraction peak at  $2\theta = 37.9^\circ$  corresponds to the (1,0,1) facet of  $\text{Mg}(\text{OH})_2$  in the brucite crystalline phase, suggesting the presence of a small amount of  $\text{Mg}(\text{OH})_2$  on the surface of 5-Na/MgO. The  $\text{Mg}(\text{OH})_2$  structure is assumed to be formed during preparation due to the high calcination temperature and moisture derived from the impregnation method.<sup>15</sup> Moreover, the 5-Na/MgO sample presents five further diffraction peaks of  $\text{NaNO}_3$ , at  $2\theta = 29.4^\circ$ ,  $31.9^\circ$ ,  $35.4^\circ$ , and  $38.9^\circ$  corresponding to

the (1,0,4), (0,0,6), (1,1,0), and (1,1,3) facets of  $\text{NaNO}_3$  in the nitratine crystalline phase, respectively. This indicates that  $\text{NaNO}_3$  remained well crystallized on the surface of MgO during this preparation. Through his research, E. S. Freeman proposed that  $\text{NaNO}_3$  could be completely decomposed at a high temperature of about  $600^\circ\text{C}$  in an inert atmosphere, while the decomposition reaction of  $\text{NaNO}_3$  in the air atmosphere would reach a certain equilibrium.<sup>40</sup> Our study proves that the remaining sodium nitrate could result from the complex reactions during the calcination (*vide infra*).

The as-prepared MgO and 5-Na/MgO samples were further investigated using the thermogravimetric-mass spectrometer in order to study their surface condition and stability. The thermogravimetric curves of the catalysts are shown in Fig. 2(a). In terms of MgO, no significant weight loss is observed even if the heating temperature reaches  $800^\circ\text{C}$ , while there is about 4% weight loss detected in 5-Na/MgO, indicating that 5-Na/MgO has relatively weak thermal stability at high temperature compared with MgO.

During the heating-up process, several molecular fractions with molecular weights  $m = 32$ ,  $44$ , and  $30$  were selected by mass spectrometry to denote the detection signals of  $\text{O}_2$ ,  $\text{CO}_2$ , and  $\text{NO}$ , respectively. The corresponding test results are shown in Fig. 2(b–d). It can be seen that the weight loss of 5-Na/MgO is mainly attributed to the decomposition of substances associated with these three gas molecules. As shown in Fig. 2(b), 5-Na/MgO showed two signal peaks of  $\text{O}_2$  in the temperature range of  $500\text{--}780^\circ\text{C}$ , which can be attributed to the decomposition of  $\text{NaNO}_3$  and  $\text{NaNO}_2$ , respectively. According to previous research,  $\text{NaNO}_3$  could undergo decomposition to produce  $\text{O}_2$  at this temperature in the inert atmosphere following reaction eqn (1), while the  $\text{NaNO}_2$  generated according to reaction eqn (1) would further decompose to produce  $\text{O}_2$  following reaction eqn (2).<sup>40,41</sup> As shown in Fig. 2(c), the  $\text{CO}_2$  signals detected in both MgO and 5-Na/MgO samples at a temperature of  $200\text{--}400^\circ\text{C}$  could be attributed to the  $\text{CO}_2$  adsorbed from the air by the

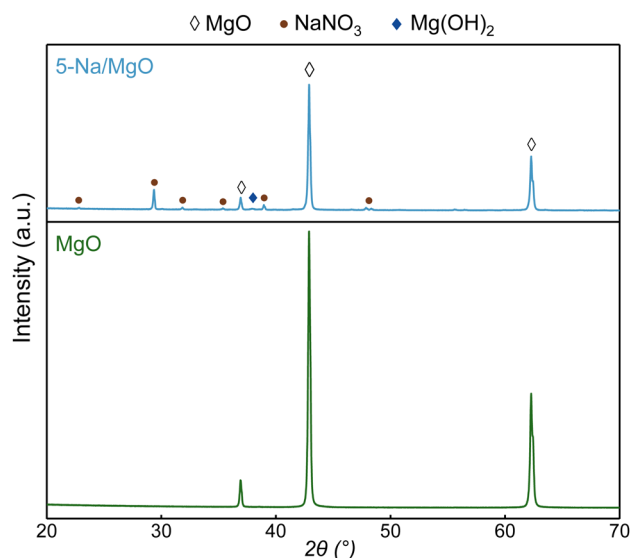


Fig. 1 XRD patterns of MgO and 5-Na/MgO.

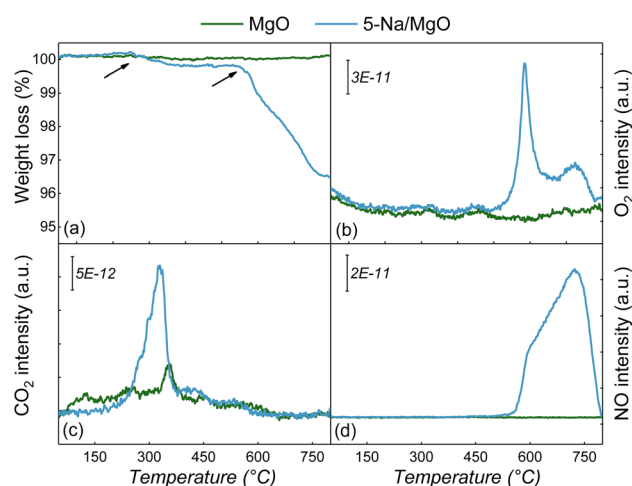


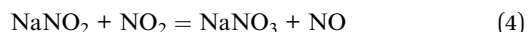
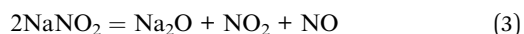
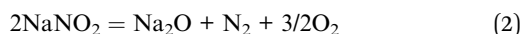
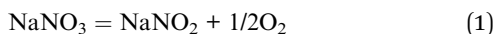
Fig. 2 TG-MS curves of MgO and 5-Na/MgO: (a) thermogravimetry, (b)  $\text{O}_2$  detection signals, (c)  $\text{CO}_2$  detection signals, (d)  $\text{NO}$  detection signals.





basic sites during storage of these catalysts. Meanwhile, both catalysts showed smaller CO<sub>2</sub> signal peaks at a temperature of 450–650 °C. Since basic substances tend to capture CO<sub>2</sub> from the air and generate the corresponding carbonate, it is hypothesized that the carbonate decomposed at this temperature.<sup>15</sup> As shown in Fig. 2(d), a large NO signal peak appeared in the temperature range of 550–800 °C for 5-Na/MgO. The formation of NO follows reaction eqn (3) and (4) and is largely attributed to the decomposition of NaNO<sub>2</sub>. It is noteworthy that the NO<sub>2</sub> produced by reaction eqn (3) would continue to react with NaNO<sub>2</sub> to form NaNO<sub>3</sub>.<sup>42</sup> The results of further XPS studies on the Na/MgO samples are shown in Fig. S2,<sup>†</sup> where it was found that the Na1s peak maximum corresponding to a binding energy at 1071.4 eV shifted to the lower binding energy region with an increase in the NaNO<sub>3</sub> loading amount, while the peak of binding energy at 1071.4 eV corresponded to the Na atoms in NaNO<sub>3</sub>, which indicated that the Na atoms had undergone an increase in electron density.<sup>43</sup> The Na1s spectrum of the Na atom of Na<sub>2</sub>O corresponds to a binding energy of 1072.5 eV, and the corresponding Na1s peaks do not appear at the position of this binding energy, suggesting that the Na species are largely in the form of NaNO<sub>3</sub>, but only a small amount of Na<sub>2</sub>O is present on the surface of the series of samples.<sup>44</sup> Then, as shown in Fig. S3,<sup>†</sup> the presence of a large amount of NaNO<sub>3</sub> was supported by further XRD studies, where the presence of NaNO<sub>3</sub> was detected on all Na/MgO samples with different loading amounts, but the diffraction peak corresponding to Na<sub>2</sub>O could not be found.

A comprehensive analysis of Fig. 2 and the above reaction equations revealed that NaNO<sub>2</sub>, as one of the products of NaNO<sub>3</sub> decomposition, could be partially converted into NaNO<sub>3</sub> again during the next step of the reaction, which confirms the above hypothesis that the presence of Na on the surface of Na/MgO is mainly in the form of NaNO<sub>3</sub>.



In order to further characterize the loading status of NaNO<sub>3</sub> on the surface of MgO, the chemical elemental distribution of 5-Na/MgO was analyzed by EDS-mapping, as shown in Fig. 3. It can be seen that the loading of NaNO<sub>3</sub> would cause agglomeration and enlargement of catalyst particles to some degree. Meanwhile, the distribution of Na and N on MgO are highly overlapped and relatively uniform at this loading amount. The results of the energy dispersive spectrum showed that the molar fractions of N and Na were 0.26% and 0.44%, respectively. This indicates that the molar ratio of N and Na is 1 : 1.69 and that there is a lot of NaNO<sub>3</sub> available on the surface of MgO.

SEM images of MgO and 5-Na/MgO are given in Fig. 4. As shown in Fig. 4(a), fresh MgO is in a homogeneous granular state and has a smooth surface, with particle diameters ranging

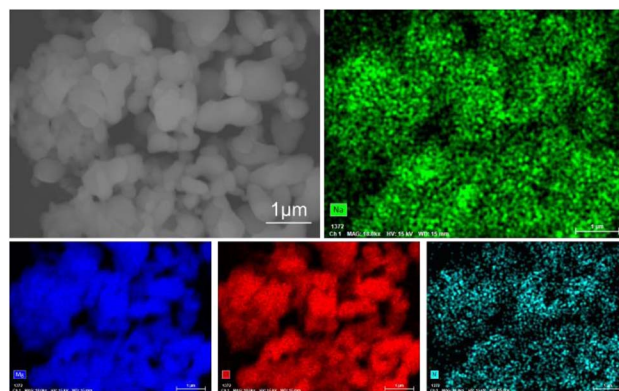


Fig. 3 SEM image and EDS-mapping of the chemical element distribution of 5-Na/MgO.

from 0.5 to 2 μm. As shown in Fig. 4(b), the loading of NaNO<sub>3</sub> resulted in a slight agglomeration of NaNO<sub>3</sub> on the surface of 5-Na/MgO with minor encapsulation of NaNO<sub>3</sub>. At the same time, the MgO support experienced partial agglomeration, resulting in larger catalyst particles with a size of 3–4 μm. The encapsulation would lead to the blockage of some of the pores when the surface of MgO is covered, resulting in a certain degree of reduction in the specific surface area and pore volume of the catalyst.

N<sub>2</sub>-adsorption and desorption isotherms were performed for the series of catalysts in order to further characterize the pore structure properties. The nitrogen adsorption–desorption isotherms and pore size distribution of the samples are shown in Fig. 5. SiO<sub>2</sub> showed a type-IV isotherm with partial mesopores.<sup>45</sup> The pores on SiO<sub>2</sub> consist predominantly of mesopores (2–50 nm) with a smaller number of other pores, while MgO contains mainly macropores. After NaNO<sub>3</sub> loading on MgO, the numbers of pores of different pore sizes were reduced to different degrees, indicating that the loading of NaNO<sub>3</sub> differentially blocked these pores. The specific surface area and microporous/remaining pore volume data of the series catalysts are shown in Table 1. It is noteworthy that NaNO<sub>3</sub> covered a large amount of the MgO surface, resulting in the specific surface area of 5-Na/MgO being even lower than that of SiO<sub>2</sub>. The total pore volumes of other pores on 5-Na/MgO decreased dramatically, suggesting that the introduction of NaNO<sub>3</sub> by the impregnation method could cause NaNO<sub>3</sub> to mainly block the mesopores and macropores on MgO. These findings further confirm the previous hypotheses.

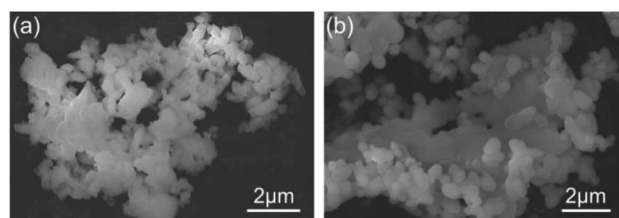


Fig. 4 SEM images of (a) MgO and (b) 5-Na/MgO.



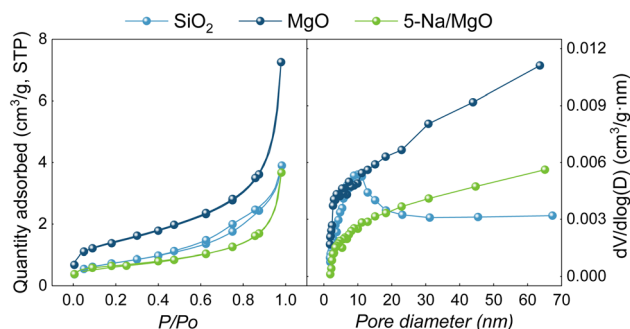


Fig. 5  $N_2$  absorption-desorption isotherm curves (left) and pore size distributions (right) of MgO and 5-Na/MgO.

In order to study the changes in basic properties of the base catalysts and to clarify the variation in their basic strength and the quantity of basic sites, the Hammett basicity index method and  $CO_2$ -TPD technology were used for further characterization and analysis, and the results are displayed in Table 1 and Fig. 6, respectively.<sup>46</sup> In 1989, Tanabe *et al.* defined a solid base with Hammett basicity index  $H_- > 26$  as a solid superbase, based on the calculation and definition of the acidity index  $H_0$  of a solid superacid.<sup>47</sup> A study also showed that the addition of Na species to MgO could provide stronger base sites with Hammett indices of 26.5–35.0.<sup>39</sup> Haznan *et al.* prepared MgO– $CeO_2$  catalysts by loading  $CeO_2$  on MgO and showed the basic strength  $H_-$  to be  $>18.4$ .<sup>48</sup> Wei *et al.* examined the basic strength of MgO/SBA-15 material using Hammett's indicator, and its  $H_-$  of 22.5 was comparable to that of bulk magnesium oxide.<sup>49</sup> The solid base catalyst prepared by loading  $NaNO_3$  onto SBA-15 had an  $H_-$  of only about 9.3 due to its structural collapse.<sup>50</sup> From the basicity index data in Table 1, it can be seen that the Hammett index of the MgO samples is greater than 18.4, which is similar to the basic strength of MgO, with Hammett indices ranging from 18.4 to 26.5 obtained from treatment under vacuum at 450 °C in ref. 38. Thus, the loading of  $NaNO_3$  on MgO significantly enhances its basicity strength, which increases from  $H_- > 18.4$  to  $H_- > 26.5$ , and the basicity strength of 5-Na/MgO reaches that of a superbase. According to Matsushashi *et al.*, the generation of superbase sites is usually attributed to the induction effect caused by electrons released from alkali metals being attracted to oxygen vacancies, and this induction effect becomes more

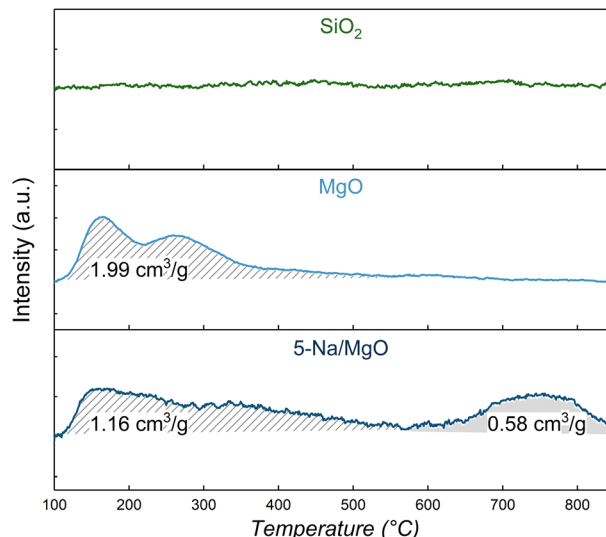


Fig. 6  $CO_2$ -TPD profiles for series samples.

pronounced when two electrons simultaneously transfer to a single vacancy.<sup>51</sup>

Since the amount of  $CO_2$  adsorbed is positively correlated with the number of basic sites, the amount of  $CO_2$  adsorbed per unit mass is labeled in Fig. 6 and was used to characterize the number of basic sites. The temperature of  $CO_2$  desorption corresponded to the strength of the basic sites and was positively correlated, so ranges of temperatures lower than 550 °C were defined as weak bases, and ranges of temperatures higher than 550 °C were defined as strong bases. None of the  $CO_2$  desorption peaks appeared on  $SiO_2$ , indicating that it was not a base catalyst but a neutral carrier. MgO showed only two  $CO_2$  desorption peaks in the low-temperature range of 110–550 °C while a total  $CO_2$  adsorption capacity of  $1.99 \text{ cm}^3 \text{ g}^{-1}$  was observed, reflecting the presence of only weakly basic sites on MgO. A total  $CO_2$  adsorption capacity of  $1.74 \text{ cm}^3 \text{ g}^{-1}$  was displayed on 5-Na/MgO, suggesting that 5-Na/MgO had fewer basic sites than MgO, which confirmed the covering of  $NaNO_3$  on the MgO surface. However, 5-Na/MgO developed a peak corresponding to stronger bases in the temperature range of 550–840 °C, indicating that the introduction of  $NaNO_3$  brought strong basic sites to the catalyst and showed a  $CO_2$  adsorption capacity of  $0.58 \text{ cm}^3 \text{ g}^{-1}$ , which was corroborated by the results of the basicity index method shown in Table 1. From analysis of

Table 1 Textual properties of the catalysts used<sup>a</sup>

Sample	Specific surface area <sup>b</sup> ( $\text{m}^2 \text{ g}^{-1}$ )	$V_{\text{micro}}^{ab}$ ( $\text{cm}^3 \text{ g}^{-1}$ )	$V_{\text{meso+macro}}^{ab}$ ( $\text{cm}^3 \text{ g}^{-1}$ )	$H_-^c$	$Na_2O^d$ (wt%)	$MgO^d$ (wt%)
$SiO_2$	2.6	<0.001	0.006	—	0	0
MgO	5.0	<0.001	0.011	>18.4	0	100
5-Na/MgO	2.4	<0.001	0.005	>26.5	1.41	98.59

<sup>a</sup>  $V_{\text{micro}}$  stands for microporous volume per unit mass of catalyst.  $V_{\text{meso+macro}}$  stands for mesoporous and macroporous volume per unit mass of catalyst. <sup>b</sup> Specific surface area was determined by the BET method.  $V_{\text{micro}}$  was calculated by the  $t$ -plot method.  $V_{\text{total}}$  stands for total pore volume of pores.  $V_{\text{meso+macro}}$  was calculated using " $V_{\text{total}} - V_{\text{micro}}$ ". Results taken from the  $N_2$  adsorbed at  $P/P_0 = 0.98$ . <sup>c</sup> Determined by the Hammett function method from Ref. Bull. Chem. Soc. Jpn. 1993, 66, 2016–2032. As described in the experimental section of this work.

<sup>d</sup> Determined by X-ray fluorescence spectrometer.

the above results, the introduction of  $\text{NaNO}_3$  provided stronger basic sites and increased the base strength of the catalyst, though partial covering of the surface of  $\text{MgO}$  led to a decrease in the number of weakly basic sites from  $1.99 \text{ cm}^3 \text{ g}^{-1}$  to  $1.16 \text{ cm}^3 \text{ g}^{-1}$ .

### 3.2 Propane catalytic cracking activity

Catalytic cracking of propane was implemented to evaluate the catalytic performance of the different catalysts. The cracking reaction over  $\text{SiO}_2$  can be considered as the thermal cracking process of a neutral catalyst, while the cracking reaction over  $\text{MgO}$  and 5- $\text{Na/MgO}$  can be reckoned as the catalytic process of solid base catalysts with different base strengths. The conversion curves of catalytic cracking of propane performed on different catalysts at different reaction temperatures are shown in Fig. 7. The propane conversions of all samples increased along with temperature. When the reaction temperature is below  $660^\circ\text{C}$ , it can be seen that the activity of the 5- $\text{Na/MgO}$  catalyst is significantly higher than that of the other catalysts. After increasing the reaction temperature to  $700^\circ\text{C}$ , the conversion of propane on  $\text{SiO}_2$  increased and exceeded that of  $\text{MgO}$ . This is consistent with the perception that thermal cracking processes generally need to be carried out at high temperatures, reflecting the features of the free radical mechanism.<sup>52</sup>

With an increase in reaction temperature, the propane conversion of the series of catalysts was enhanced to different degrees. Among them, the catalytic activity of 5- $\text{Na/MgO}$  showed the greatest improvement, with the conversion increasing from 4.1% to more than 21%. The conversion of 5- $\text{Na/MgO}$  was increased by about 2.5% at a reaction temperature of  $580^\circ\text{C}$  compared to that of  $\text{MgO}$ , and by about 11% at a reaction temperature of  $700^\circ\text{C}$ . The above results suggest that  $\text{MgO}$  with weaker basic strength could not significantly improve the catalytic performance for the catalytic cracking reaction of

propane, while the 5- $\text{Na/MgO}$  catalyst with stronger basicity showed significantly better catalytic performance. 5- $\text{Na/MgO}$  might have a lower activation energy barrier for catalytic cracking than the other catalysts, showing a noticeable advantage provided by the stronger base site.

In order to study the differences in the series of catalysts in catalytic cracking and their role in increasing the production of light olefins, the product distributions of the series of catalysts were further analyzed and compared. The product distribution of the catalytic cracking reaction of propane over the series of catalysts is shown in Fig. 8. As shown in Fig. 8(a), the  $\text{H}_2$  selectivity of  $\text{SiO}_2$  and  $\text{MgO}$  catalysts increased rapidly with the increase in reaction temperature, and the positive correlation between  $\text{H}_2$  selectivity and reaction temperature indicated that these catalysts tended to generate more  $\text{H}_2$  at high temperatures, and that this process might lead to competitive adsorption of  $\text{H}_2$  on the surface of the catalysts, which in turn would inhibit the conversion of the reaction and the yield of light olefins. In contrast, the selectivity for  $\text{H}_2$  is much lower than that of  $\text{SiO}_2$  and  $\text{MgO}$  and is stabilized using 5- $\text{Na/MgO}$  as catalyst. With the increase in reaction temperature, the selectivity for  $\text{H}_2$  did not show a positive correlation with reaction temperature, and even decreased to a certain extent with the increase in reaction temperature, implying that a new catalytic process different from that of the  $\text{SiO}_2$  or  $\text{MgO}$  catalysts could be developed on the 5- $\text{Na/MgO}$  catalyst. As shown in Fig. 8(b),  $\text{SiO}_2$  had the lowest  $\text{CH}_4$  selectivity followed by 5- $\text{Na/MgO}$  at a reaction temperature of  $580^\circ\text{C}$ . However, the  $\text{CH}_4$  selectivity on  $\text{SiO}_2$  and  $\text{MgO}$  catalysts increased rapidly with the raising of the reaction temperature. Although there was an increase in  $\text{CH}_4$  selectivity on 5- $\text{Na/MgO}$ , the increment was minimal compared to that of the other catalysts. When the reaction temperature was  $600\text{--}700^\circ\text{C}$ , the  $\text{CH}_4$  selectivity on 5- $\text{Na/MgO}$  was significantly lower than that on the other catalysts and the  $\text{CH}_4$  selectivity on 5- $\text{Na/MgO}$  was relatively unchanged in this temperature range, and the comparison of these results reflected that the 5- $\text{Na/MgO}$  catalysts had a good performance of

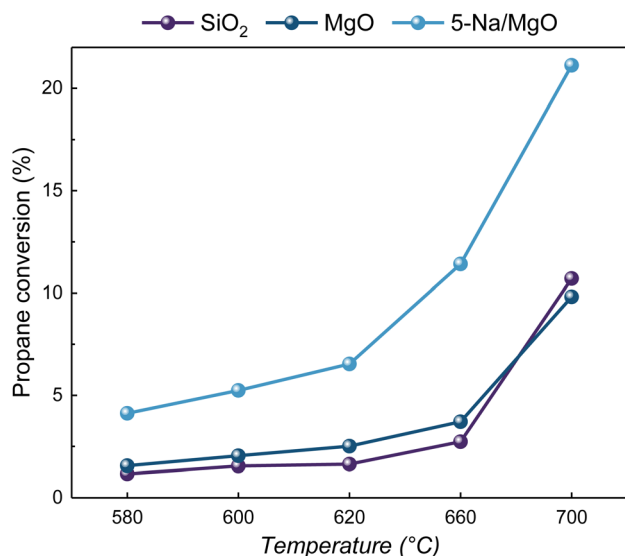


Fig. 7 Propane conversion of series catalysts.

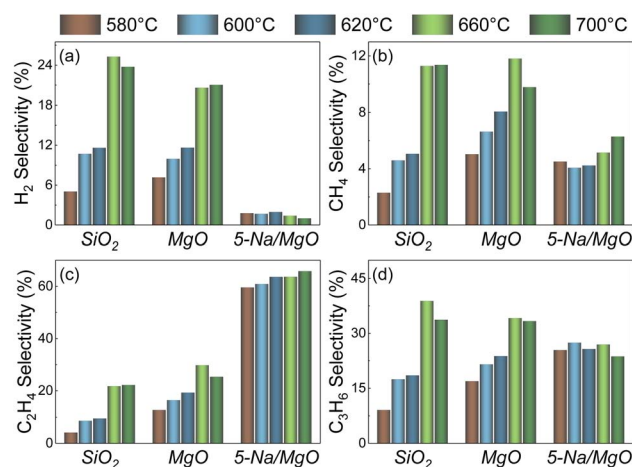


Fig. 8 Catalytic cracking performance for the catalysts at different temperatures: (a)  $\text{H}_2$  selectivity, (b)  $\text{CH}_4$  selectivity, (c)  $\text{C}_2\text{H}_4$  selectivity, (d)  $\text{C}_3\text{H}_6$  selectivity.



inhibiting  $\text{CH}_4$  production. In the product distributions shown in Fig. 8, the 5-Na/MgO catalyst is clearly distinguishable from the other catalysts by the  $\text{C}_2\text{H}_4$  selectivity in addition to the  $\text{H}_2$  selectivity, and the  $\text{C}_2\text{H}_4$  selectivity of the three types of catalysts at different reaction temperatures are shown in Fig. 8(c). Remarkably, the  $\text{C}_2\text{H}_4$  selectivity of the 5-Na/MgO catalyst reached 59.56% at 580 °C, which was about three times higher than that of  $\text{SiO}_2$ , whereas the  $\text{C}_2\text{H}_4$  selectivities of the  $\text{SiO}_2$  and MgO catalysts were only 4.07% and 12.74%, respectively, which clearly demonstrated that the mechanism of propane catalytic cracking was different on 5-Na/MgO compared to the other catalysts. With the increase in reaction temperature, the  $\text{C}_2\text{H}_4$  selectivity of the three types of catalyst increased to a certain extent, but the increase was not significant. The  $\text{C}_2\text{H}_4$  selectivity on the 5-Na/MgO catalyst is maintained at more than 60%, whereas the highest  $\text{C}_2\text{H}_4$  selectivity achieved by the other catalysts is only 29.74% of that of the MgO catalyst at 660 °C, which indicates that the 5-Na/MgO catalyst showed superior promotion of  $\text{C}_2\text{H}_4$  production. This indicates that the 5-Na/MgO catalyst has better catalytic performance, and that the use of this kind of catalyst could radically change the product distribution of the propane catalytic cracking reaction to maximize the production of ethylene. The  $\text{C}_3\text{H}_6$  selectivity of the series of catalysts is shown in Fig. 8(d), and 5-Na/MgO had the highest  $\text{C}_3\text{H}_6$  selectivity at a reaction temperature of 580 °C. However, the differences in  $\text{C}_3\text{H}_6$  selectivity among the three types of catalyst kept narrowing as the reaction temperature increased. The  $\text{C}_3\text{H}_6$  selectivities of  $\text{SiO}_2$  and MgO slightly increase, while the  $\text{C}_3\text{H}_6$  selectivity of 5-Na/MgO shows no significant increase or decrease. The above results show that the 5-Na/MgO catalyst has better  $\text{C}_2\text{H}_4$  selectivity and lower  $\text{H}_2$  and  $\text{CH}_4$  selectivity, which can provide a more reasonable product distribution for the propane catalytic cracking reaction.

Through the above analysis, the 5-Na/MgO catalysts showed significant differences in terms of catalytic performance over the other catalysts. Therefore, the catalytic properties of the three types of catalyst were further investigated by comprehensive analysis of different products, as shown in Fig. 9. As can be seen from Fig. 9(a), with the increase in reaction temperature, 5-Na/MgO maintained the highest light olefin selectivity, followed by MgO. The light olefin selectivity of 5-Na/MgO

reached 91.7% at 660 °C and there was almost a positive correlation between the light olefin selectivity of the three catalysts and the reaction temperature. In conclusion, the catalytic cracking of propane using the 5-Na/MgO catalyst produced mainly a large number of light olefins and a small number of other products. Meanwhile, the performance of the 5-Na/MgO catalyst in producing light olefins was more stable than that of the other catalysts in terms of temperature change, and the product distribution showed less sensitivity to temperature.

The higher selectivity for ethylene than for propylene is a feature of thermal cracking and base-catalyzed processes.<sup>53–56</sup> Therefore,  $\text{C}_2\text{H}_4$  selectivity/ $\text{C}_3\text{H}_6$  selectivity was defined to probe the product properties of base catalysis. The  $\text{C}_2\text{H}_4$  selectivity/ $\text{C}_3\text{H}_6$  selectivity for various catalysts at different reaction temperatures is shown in Fig. 9(b). It can be seen that the ratio was relatively stable over the three types of catalyst, and it was consistently lower than 1 over  $\text{SiO}_2$  and MgO and consistently higher than 2 over 5-Na/MgO.

The thermal cracking process of propane does not yield a product distribution consistent with the free radical mechanism in the temperature range of 580–700 °C in this paper, and its  $\text{C}_2\text{H}_4$  selectivity/ $\text{C}_3\text{H}_6$  selectivity is also less than 1. Although this ratio increases slowly with rising temperature on  $\text{SiO}_2$ , the ratio is only equal to that of MgO when the reaction temperature increases to 700 °C. According to the product distribution on  $\text{SiO}_2$  shown in Fig. 8, it could be seen that with the increase in reaction temperature, the selectivities for  $\text{H}_2$  and  $\text{C}_3\text{H}_6$  change with the same trend, while the  $\text{CH}_4$  and  $\text{C}_2\text{H}_4$  change with another trend. The selectivity for  $\text{C}_3\text{H}_6$  is significantly higher than for the other products. Therefore, a possible explanation is provided by the following: small alkane molecules such as propane molecules are thermodynamically more stable than long-chain alkanes, resulting in a higher activation energy for propane cracking, suggesting that there is a higher incidence of primary scission of propane molecules over  $\text{SiO}_2$  in the reaction temperature range of 580–700 °C. The propane molecule generates methyl and ethyl radicals mainly by C–C bond breaking *via* a free radical mechanism, and these two radicals could not be further cracked by  $\beta$ -scission. Propylene could be produced only by dehydrogenation of propane or by a subsequent reaction based on the cracking of propane to generate a small amount of hydrogen radicals and propyl radicals, while ethylene would be even less available as the product of the subsequent reaction. This is reflected in the lower conversion, as shown in Fig. 7, which in turn affects the product distribution. Currently, the operating temperatures of commonly used thermal cracking processes would typically be  $\geq 800$  °C, and since the initiation of free radicals is known to be a rate-controlling step in the free radical reaction, the above results might also be attributed to the low reaction temperature used in this work.<sup>4,5,24</sup> The MgO catalysts with lower basic strength than 5-Na/MgO had the second highest  $\text{C}_2\text{H}_4$  selectivity/ $\text{C}_3\text{H}_6$  selectivity ratio, which remained stable at around 0.8. It is hypothesized that the fact that MgO did not exhibit typical base-catalytic features might be attributed to the weaker base strength. In particular, the  $\text{C}_2\text{H}_4$  selectivity/ $\text{C}_3\text{H}_6$  selectivity ratio

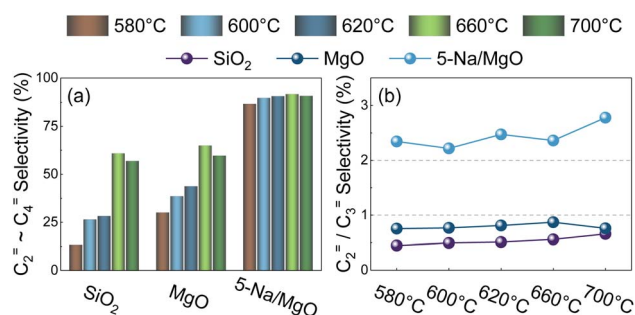


Fig. 9 Products analysis for the catalysts at different temperatures: (a) summation of  $\text{C}_2 = \sim \text{C}_4 =$  (light olefin) selectivity, (b)  $\text{C}_2\text{H}_4$  selectivity/ $\text{C}_3\text{H}_6$  selectivity.



on 5-Na/MgO was stable at greater than 2 with a slowly increasing trend. Meanwhile, 5-Na/MgO provided the highest light olefin selectivity, suggesting that these catalysts were beneficial for the generation of low-carbon olefins and could potentially undergo fewer hydrogen-transfer reactions and condensation reactions, which could significantly facilitate the generation of  $C_2H_4$  and provide a completely different reaction pathway for the catalytic cracking of propane.

In summary, by evaluating the performance of the series of catalysts at different reaction temperatures, the significant variation in product distribution reflected the difference in the reaction mechanisms on the neutral and base catalysts. The product distribution of the 5-Na/MgO catalyst was obviously better than that of the other catalysts, and the product distribution was relatively stable at different reaction temperatures, suggesting that the catalytic process of 5-Na/MgO may follow a new mechanism that may be insensitive to temperature and significantly different from the thermal cracking process.

### 3.3 Effect of Na content on basicity and catalytic properties

To investigate the effect of Na content on the catalytic properties, Na-loaded MgO samples with different loading amounts were tested for the propane cracking reaction at different temperatures. The propane conversion curves of  $NaNO_3$ -loaded samples at a series of reaction temperatures are shown in Fig. 10. As can be seen from Fig. 10, the conversion of all Na/MgO samples increased to a certain extent with the increase in reaction temperature, which is consistent with the realization that molecular cracking is a heat-absorbing reaction. Meanwhile, the propane conversion of Na/MgO samples at a series of reaction temperatures all showed a tendency to increase and then decrease with an increase in Na loading amount, with almost identical trends, and the 5-Na/MgO sample provided the optimal reaction activity amongst all of them. It is noteworthy that, although the catalytic performance of the samples

decreased with an increase in loading after the loading amount exceeded 5%, they were all better than those of the samples without Na loading. This suggests that such a change in propane conversion may not be related directly to the change in the coverage of the surface or in the number of basic sites (like  $Na_2O$ ), but is more likely to be related to the chemical and electrical environments of the active sites provided by the  $NaNO_3$  loading on MgO.<sup>39</sup>

In order to investigate the basic properties of the Na/MgO samples, the series of catalysts prepared by  $NaNO_3$  impregnation were characterized for  $CO_2$ -TPD, and the results of the characterization are shown in Fig. S4.† It can clearly be seen that with the increase in Na loading, the Na/MgO sample started to show obvious high-temperature desorption peaks of  $CO_2$ , which corresponded to the strong base sites. Upon further increasing the  $NaNO_3$  loading amount, the peak temperature of the high-temperature desorption peaks started to shift towards a higher temperature, which indicated the positive correlation between the  $NaNO_3$  loading amount and the basicity strength. It is noteworthy that the Na/MgO samples showed fluctuations in the relationship between the area of their high-temperature desorption peaks and the loading amount of  $NaNO_3$ , with the areas of the high-temperature desorption peaks (labelled (1), (2), and (3) in the figure, respectively) on 5-Na/MgO, 10-Na/MgO, and 15-Na/MgO being 285.70, 281.58, and 191.72, respectively, and the 15-Na/MgO sample also showed a  $CO_2$  desorption peak corresponding to medium-strong base sites in the temperature range of 500–550 °C. Thus, there were no strong base sites on the MgO sample and the 1-Na/MgO sample; the 5-Na/MgO sample and the 10-Na/MgO sample have similar amounts of strong base sites; whereas the quantity of sites corresponding to a strong base on the 15-Na/MgO sample had decreased. Thus, the increase in  $NaNO_3$  loading amount is able to provide more strongly basic sites within a certain limit. The amount of strong base sites will decrease if this limit is exceeded, and some of the strong base sites may be converted to medium-strong base sites.

In summary, in order to investigate the effect of different types of catalyst on the propane cracking performance and reaction mechanism, Na/MgO samples were chosen for comparison with MgO and a subsequent DFT calculation study.

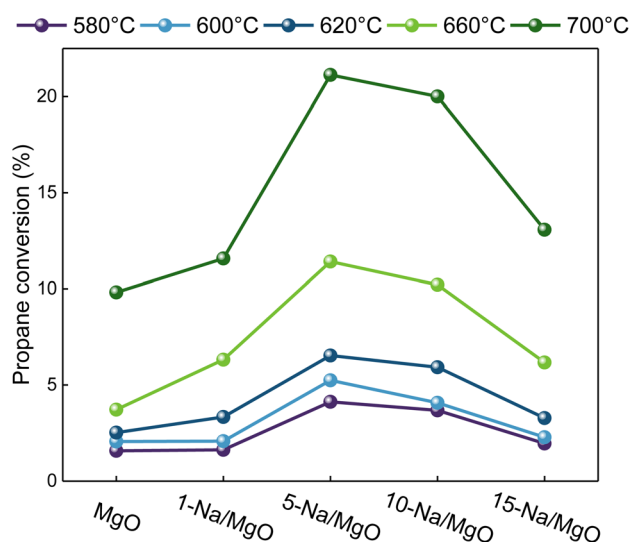
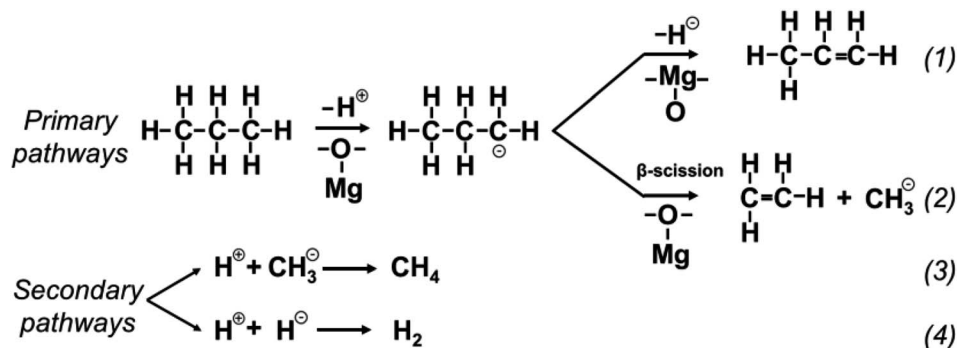


Fig. 10 Propane conversion of Na/MgO samples at a series of reaction temperatures.

### 3.4 Pathway of propane to light olefins via catalytic cracking

Depending on the reaction temperature and catalyst, the mechanism of generation of light olefins from propane might change to a greater or lesser extent, which could be reflected in the product distribution. As mentioned above, Na/MgO catalysts demonstrated particular advantages when used in the catalytic cracking reaction of propane, not only in terms of improved conversion, but also in terms of a more reasonable product distribution. Therefore, the following reaction pathway for Na/MgO-catalyzed propane cracking was proposed based on the distribution features of the products at different temperatures, as shown in Scheme 1. Path (2) was the dominant path for the Na/MgO catalyst, and this path accounted for the largest portion of the catalytic cracking of propane, which in turn produced a large amount of ethylene. A smaller amount of



Scheme 1 Reaction pathways of catalytic cracking of propane on Na/MgO.

propylene was generated through path (1). The process described above is the primary path of the propane catalytic cracking reaction, and the advantage of the Na/MgO catalyst might be reflected in path (2) with a lower activation energy barrier, and the ratio of these two paths directly determined the final catalytic performance. Subsequent reduction of the carbanions proceeded *via* paths (3) and (4) to produce less  $\text{H}_2$  and  $\text{CH}_4$ . The compounds of  $\text{C}_4$  both had low selectivity over the catalysts and were therefore not considered the main reaction. It should be noted that there should be more reaction paths in the secondary reaction rather than being limited to those listed in the figure, which yielded further small amounts of other products with a minimal fraction in the reaction process. Therefore, in order to verify the feasibility and reasonability of the proposed reaction pathways, the charge distribution on the surface of the solid base catalysts and their paths catalyzing the cracking of propane molecules were calculated.

### 3.5 The effect of catalyst surface on reaction performance

Clarification of the catalytic mechanism plays an important role in the regulation of the catalytic reaction process. The mainstream view of the catalytic cracking mechanism of hydrocarbon molecules in the base-catalyzed process includes the free radical mechanism or the carbanion mechanism, but awareness of these two mechanisms was still ambiguous.<sup>53–56</sup> In order to investigate the surface properties of solid base catalysts, the electronic structure of propane, and the effect of solid base catalysts on the distribution of hydrocarbon catalytic cracking products, the charge distribution on the surface of solid base catalysts and their pathways of catalytic cracking of propane were investigated in this study using density functional theory (DFT).

**3.5.1 The charge variation on the base catalyst surface.** The electronic structure of propane is shown in Fig. S5.† The highest occupied molecular orbital mainly resides in the C–H bond of the propane molecule, which serves as a relatively active reactive site. The carbon atom has greater electronegativity, resulting in a greater electron shift in favor of the carbon atom. According to the results of XRD, the (2,0,0) facets of MgO are the dominant facets with the highest percentage. Therefore, in order to study the electronic structure of the catalyst surface, charge distribution analysis and electric potential calculation were applied

to the MgO and Na/MgO surfaces based on the (2,0,0) facets of MgO as a typical facet, as shown in Fig. 11. The loading of  $\text{NaNO}_3$  on the surface of MgO significantly changed the electrical properties of the MgO surface. Giamello *et al.* suggested that the introduction of alkali metals caused changes in the F centers of lattice oxygen. Upon introduction of alkali metals into metal oxides, the alkali metal would release electrons, which would normally be attracted to the defective positions of the oxide lattice like oxygen vacancies ( $\text{F}^+$  centers).<sup>57</sup> As shown in Fig. 11(a, c and d), the negative charges of N and O on  $\text{NaNO}_3$  decreased while the negative charge of lattice oxygen on the surface of magnesium oxide located near  $\text{NaNO}_3$  increased to some degree, with the charge falling from around  $-0.426$  to  $-0.43$ . In Fig. 11(b and e), the blue part of the data bar indicates the electron-enriched state and the red color indicates the electron-deficient state. It can be seen that the charge transfer between  $\text{NaNO}_3$  and MgO leads to some increase in the electron cloud density of the lattice oxygen on the surface of MgO located in the vicinity of  $\text{NaNO}_3$ , which shows an electron-rich state, and is thus more likely to provide base sites for the adsorption and activation of propane molecules.

As mentioned above, the presence of  $\text{NaNO}_3$  on the catalyst surface changed the charge distribution, making it easier for propane molecules to adsorb on the MgO surface, thus facilitating the catalytic cracking reaction of propane. The adsorption energy of propane molecules was analyzed in order to study the states of propane molecules after adsorption on the Na/MgO surface. The top view, side view and adsorption energy values of the propane molecules in different adsorption conformations when adsorbed on  $\text{NaNO}_3$  or on MgO adjacent to  $\text{NaNO}_3$  are shown in Fig. 12. The adsorption energy of propane molecules adsorbed on  $\text{NaNO}_3$  on Na/MgO was  $-17.1$  to  $-31.8$   $\text{kJ mol}^{-1}$ , while the adsorption energy of propane molecules adsorbed on the MgO surface adjacent to  $\text{NaNO}_3$  was  $-44.6$  to  $-45.0$   $\text{kJ mol}^{-1}$ . Based on the results of adsorption energy calculations, it can be concluded that propane molecules preferred to adsorb on the MgO surface adjacent to  $\text{NaNO}_3$  rather than tending to adsorb on  $\text{NaNO}_3$  when approaching the surface of Na/MgO. Meanwhile, the introduction of  $\text{NaNO}_3$  made the propane molecules more likely to adsorb on the MgO surface to facilitate the catalytic cracking reaction of propane. In addition, Matsushashi *et al.* studied a series of solid base



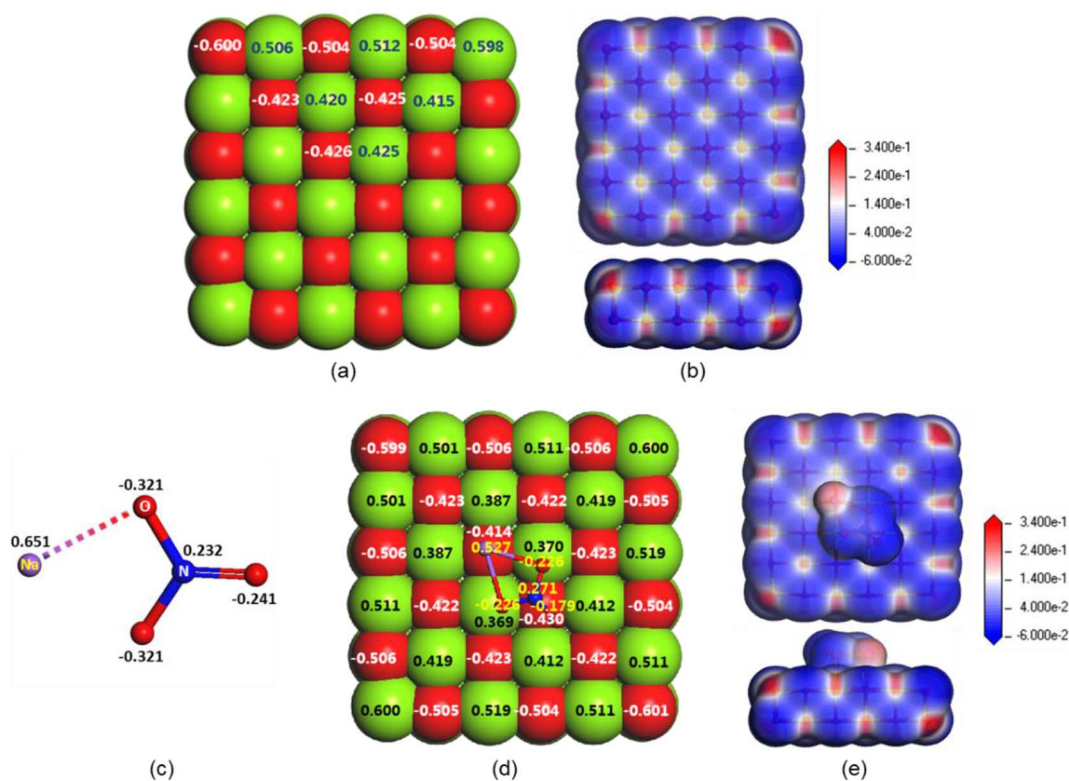


Fig. 11 The local charge distribution of (a) MgO, (c) NaNO<sub>3</sub> and (d) Na/MgO. The electric potential distribution of (b) MgO and (e) Na/MgO. The green and red colored spheres denote Mg and O, respectively.

catalysts and concluded that the inductive effect resulting from electrons released from alkali metals being attracted to oxygen vacancies promoted basic catalytic activity, rather than Na<sup>+</sup> or K<sup>+</sup> species.<sup>58</sup> Combined with analysis of the calculations, the catalytic cracking for propane on Na/MgO still proceeded on the surface of MgO rather than on NaNO<sub>3</sub>.

**3.5.2 Speculation about the pathway for propane catalytic cracking on solid base catalysts.** As hypothesized in the above section on product distribution, the catalytic cracking process for propane should be significantly different when performed over the two types of catalyst, MgO and Na/MgO, and the

process was conducted on the surface of MgO. Therefore, the surface states of MgO and Na/MgO were selected for the calculation of the pathway of the catalytic cracking reaction of propane. The preliminary reaction pathways when propane molecules were adsorbed on the surface-active sites of MgO and Na/MgO are shown in Fig. 13. The first reaction step of a propane molecule adsorbed on both catalysts occurred with the seizure of hydrogen by the MgO lattice oxygen, which resulted in the propane molecule firstly undergoing molecular-terminal C-H bond scission and then the generation of a propyl-carbanion and an adsorbed H proton (Fig. 13(a))

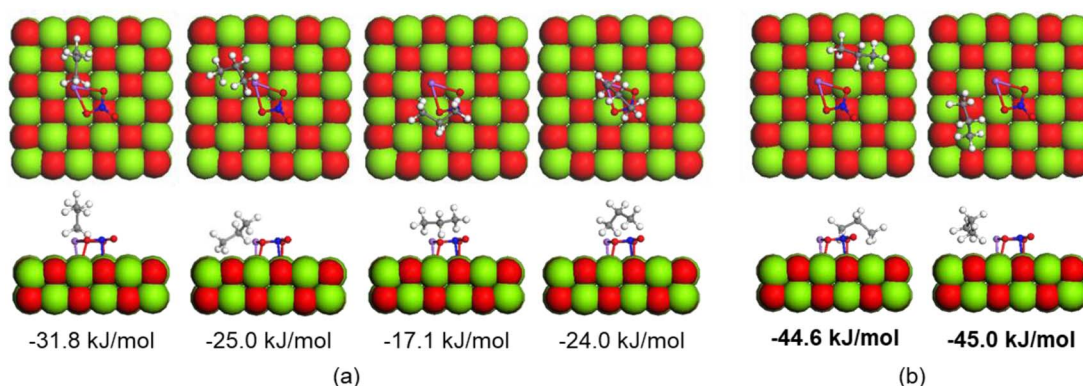


Fig. 12 The adsorption energies of propane molecules in different molecular conformations after adsorption at different positions on the Na/MgO surface: (a) adsorbed on NaNO<sub>3</sub>, (b) adsorbed on the MgO surface lattice oxygen adjacent to NaNO<sub>3</sub>.



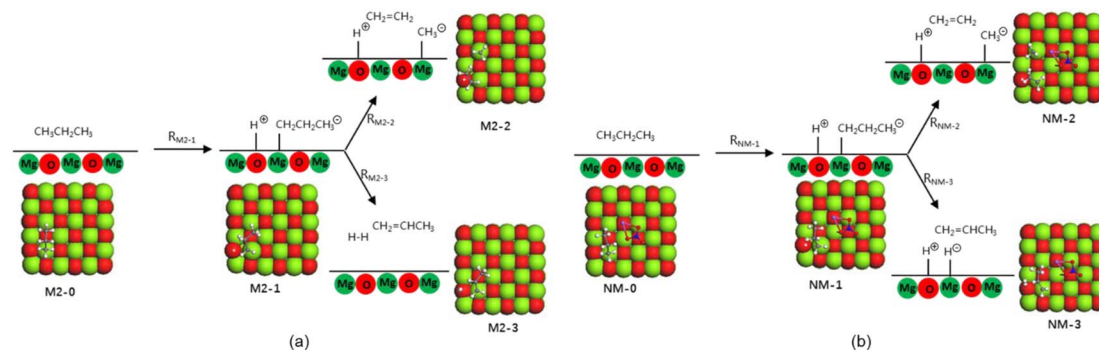


Fig. 13 Different pathways on the surface of (a) MgO and (b) Na/MgO.

reaction path  $R_{M2-1}$ , Fig. 13(b) reaction path  $R_{NM-1}$ ). Differences in the catalytic cracking reactions of propane on MgO and Na/MgO start to appear in the subsequent second step of the reaction. On MgO, the propyl-carbanion would continue to adsorb on the catalyst surface to undergo  $\beta$ -scission of the C-C bond to generate ethylene and a methyl-carbanion (Fig. 13(a) reaction path  $R_{M2-2}$ ), or dehydrogenation of the propyl-carbanion and the generation of propylene and hydrogen with protons adsorbed on the catalyst surface (Fig. 13(a) reaction path  $R_{M2-3}$ ). On the Na/MgO catalyst, the propyl-carbanion would continue to adsorb on the catalyst surface to undergo  $\beta$ -scission of the C-C bond to generate ethylene and the methyl-carbanion (Fig. 13(a) reaction pathway  $R_{NM-2}$ ), or the seizure of the hydrogen of the propyl-carbanion by the Mg atom on the catalyst surface to generate propylene (Fig. 13(a) reaction pathway  $R_{NM-3}$ ). Therefore, the production and conversion of the intermediate carbanions resulted in the catalytic cracking processes on the base catalyst being distinct from the other catalysts in terms of mechanism. At the same time, MgO provided higher  $H_2$  selectivity than Na/MgO, as described in Section 2, and the above analysis well explained why this difference emerged.

The changes in system energy for the reaction processes (as shown in the reaction path in Fig. 13) on both MgO and Na/MgO catalysts are shown in Fig. 14. In propane adsorption in the first step of the reaction (M2-0 and NM-0 in Fig. 14), Na/MgO could provide a lower adsorption energy for the adsorption of propane molecules compared to MgO, which makes the propane molecules more easily activated for the next step of the reaction. In the second step of the reaction, the energy barriers for the hydrogen proton capture reactions of the lattice oxygens of MgO and Na/MgO (M2-1 and NM-1 in Fig. 14) proceeded with  $212.6 \text{ kJ mol}^{-1}$  and  $198.8 \text{ kJ mol}^{-1}$ , respectively, suggesting that the introduction of  $NaNO_3$  made it easier to break the terminal C-H bond of the propane molecule and produce the propyl-carbanion. The improved conversion of Na/MgO compared to MgO in the results of the catalyst evaluation in Section 2 provided support for this view. It is noteworthy that the reaction energy barriers of the reaction pathways  $R_{M2-2}$  and  $R_{M2-3}$  on MgO were  $272.1 \text{ kJ mol}^{-1}$  and  $139.9 \text{ kJ mol}^{-1}$ , respectively, when the propyl-carbanion proceeded to the next step of the reaction. The pathways  $R_{M2-2}$  or  $R_{M2-3}$  corresponded to the production of ethylene or propylene and hydrogen, respectively. Therefore,

the cracking of propyl-carbanions on MgO was more favorable for the production of propylene and hydrogen rather than ethylene *via*  $\beta$ -scission, and this conclusion was confirmed by

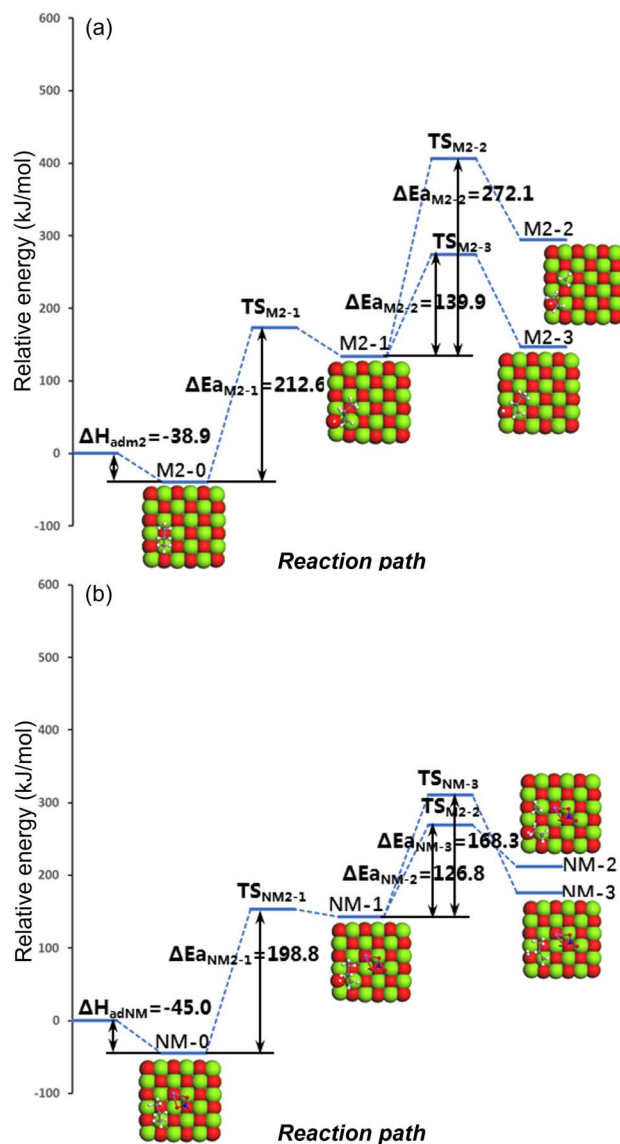


Fig. 14 System energy variation during the reaction on (a) MgO and (b) Na/MgO.





the results of the catalytic performance of MgO. Unlike MgO, the reaction energy barriers for the reaction paths  $R_{\text{NM-2}}$  and  $R_{\text{NM-3}}$  on Na/MgO were 126.8 kJ mol<sup>-1</sup> and 168.3 kJ mol<sup>-1</sup>, respectively, whereas paths  $R_{\text{NM-2}}$  and  $R_{\text{NM-3}}$  corresponded to the production of ethylene and propylene, respectively. Therefore, it was easier to generate ethylene *via*  $\beta$ -scission of the propyl-carbanion over Na/MgO. From the catalytic performances of Na/MgO and MgO, it could be concluded that the introduction of NaNO<sub>3</sub> to MgO increased the selectivity ratio of C<sub>2</sub>H<sub>4</sub> to C<sub>3</sub>H<sub>6</sub> from about 0.8 to about 2.3, and about 90% of the total light olefin selectivity was obtained, which confirmed the conclusions of the reaction pathway drawn through simulations.

## 4. Conclusions

In this work, the cracking of propane molecules *via* a thermal cracking process, a base-catalyzed process, and a strong-base-catalyzed process were studied by means of catalyst characterization and evaluation of catalyst performance. Then, a series of samples with different Na contents were analyzed during the propane cracking reaction at different temperatures. Subsequently, density functional theory (DFT) simulations were performed for the MgO and Na/MgO catalysts. An analysis of the structure–activity relationship between catalyst and reaction performance and the mechanism of catalytic cracking of propane by the base-catalyzed process led to the following conclusions: the basic strength of the samples increased slightly with the rise in Na content, but the trend in the quantity of strong base sites did not follow the trend of the Na-loading amount. Moreover, the conversion rates of the samples showed a “volcano” distribution with increasing Na content, indicating that the active sites of propane cracking were not only limited to the base sites (Na<sub>2</sub>O), but could be found on generated composite basic active centers. The favored active sites for propane cracking to light olefins are the superbase sites, which show better cracking performance and product distribution, as evidenced by the significant improvement in propane conversion and light olefin selectivity with the introduction of stronger base sites. The introduction of NaNO<sub>3</sub> could alter the charge distribution condition of the catalyst, introducing a different active site for the MgO surface through charge transfer, which was generated from the interaction between NaNO<sub>3</sub> and MgO and reflected in the obvious enhancement of the base strength and the significant difference in the reaction routes. 5-Na/MgO generates a different reaction mechanism in the reaction process from MgO and SiO<sub>2</sub>, which reduces the energy barriers of the reaction as well as the activation energy of the adsorption process of propane molecules and the activation energy of  $\beta$ -scission under the carbanion mechanism, which in turn improves the selectivity for ethylene to inhibit the generation of such unwelcome processes, *e.g.*, the production of H<sub>2</sub> and CH<sub>4</sub>, and condensation reactions.

## Conflicts of interest

There are no conflicts to declare.

## Acknowledgements

This work is financially supported by the National Key Research and Development Program of China (grant number 2022YFB3504000) and the Contract Projects of China Petroleum & Chemical Corporation (SINOPEC Corp.) [grant number 123031].

## Notes and references

- 1 T. Ren, M. Patel and K. Blok, *Energy*, 2006, **31**, 425–451.
- 2 Z. Li, H. Wang, G. Huang, W. Ren, B. Zhang and S. Wei, *Chem. Ind. Eng. Prog.*, 2017, **36**, 767–773.
- 3 A. Akah, J. Williams and M. Ghrami, *Catal. Surv. Asia*, 2019, **23**, 265–276.
- 4 H. Wang, *Chem. Ind. Eng. Prog.*, 2020, **39**, 4401–4407.
- 5 A. Akah and M. Al-Ghrami, *Appl. Petrochem. Res.*, 2015, **5**, 377–392.
- 6 A. Tanimu, G. Tanimu, H. Alasiri and A. Aitani, *Energy Fuels*, 2022, **36**, 5152–5166.
- 7 M. A. Alabdullah, A. R. Gomez, J. Vittenet, A. Bendjeriou-Sedjerari, W. Xu, I. A. Abba and J. Gascon, *ACS Catal.*, 2020, **10**, 8131–8140.
- 8 S. M. Sadrameli, *Fuel*, 2016, **173**, 285–297.
- 9 L. Li, J. Gao, C. Xu and X. Meng, *Chem. Eng. J.*, 2006, **116**, 155–161.
- 10 S. M. Jeong, J. H. Chae, J. Kang, S. H. Lee and W. Lee, *Catal. Today*, 2002, **74**, 257–264.
- 11 A. Corma, E. Corresa, Y. Mathieu, L. Sauvanaud, S. Al-Bogami, M. S. Al-Ghrami and A. Bourane, *Catal. Sci. Technol.*, 2017, **7**, 12–46.
- 12 X. Meng, C. Xu, J. Gao and L. Li, *Appl. Catal., A*, 2005, **294**, 168–176.
- 13 W. Rongbin, *Acta Pet. Sin.*, 2021, **37**, 384.
- 14 R. Pujro, M. Falco and U. Sedran, *J. Chem. Technol. Biotechnol.*, 2016, **91**, 336–345.
- 15 Y. Ono and H. Hattori, *Solid Base Catalysis*, Springer Science & Business Media, Germany, 2012.
- 16 T. Wei, M. H. Wang, W. Wei, Y. H. Sun and B. Zhong, *Chem.–Eur. J.*, 2002, **65**, 594–600.
- 17 X. Z. Li and Q. Jiang, *Low Carbon Chem. Chem. Eng.*, 2005, **30**, 42–48.
- 18 V. Verdoliva, M. Saviano and S. De Luca, *Catalysts*, 2019, **9**, 248.
- 19 X. Gong, M. Caglayan, Y. Ye, K. Liu, J. Gascon and A. Dutta Chowdhury, *Chem. Rev.*, 2022, **122**, 14275–14345.
- 20 M. Boronat, M. J. Climent, P. Concepción, U. Díaz, H. García, S. Iborra, A. Leyva-Pérez, L. Liu, A. Martínez and C. Martínez, *ACS Catal.*, 2022, **12**, 7054–7123.
- 21 A. Munyentwali, H. Li and Q. Yang, *Appl. Catal., A*, 2022, **633**, 118525.
- 22 P. Gupta and S. Paul, *Catal. Today*, 2014, **236**, 153–170.
- 23 C. Boyadjian, L. Lefferts and K. Seshan, *Appl. Catal., A*, 2010, **372**, 167–174.
- 24 B. Basu and D. Kunzru, *Ind. Eng. Chem. Res.*, 1992, **31**, 146–155.



- 25 R. Tang, Y. Tian, G. Leng and Y. Qiao, *Acta Pet. Sin.*, 2016, **32**, 486–492.
- 26 Y. Zhang, D. Yu, W. Li, Y. Wang, S. Gao and G. Xu, *Ind. Eng. Chem. Res.*, 2012, **51**, 15032–15040.
- 27 M. S. Gao, G. H. Zhang, L. Zhao, J. S. Gao and C. M. Xu, *Ind. Eng. Chem. Res.*, 2023, **62**, 1215–1226.
- 28 M. L. Kaliya and S. B. Kogan, *Catal. Today*, 2005, **106**, 95–98.
- 29 S. M. Jeong, J. H. Chae and W. H. Lee, *Ind. Eng. Chem. Res.*, 2001, **40**, 6081–6086.
- 30 N. Niwamanya, J. Zhang, C. Gao, D. T. Sekyere, A. Barigye, J. Nangendo and Y. Tian, *Fuel*, 2022, **328**, 125285.
- 31 R. Y. Tang, Y. Y. Tian, J. L. Cai and Y. Y. Qiao, *Chem. Eng. Oil Gas*, 2015, **44**, 23–27.
- 32 R. Y. Tang, Y. Y. Tian, Y. Y. Qiao, G. M. Zhao and H. F. Zhou, *Energy Fuels*, 2016, **30**, 8855–8862.
- 33 Y. Y. Tian, Y. J. Che, M. S. Chen, W. Feng, J. H. Zhang and Y. Y. Qiao, *Energy Fuels*, 2019, **33**, 7297–7304.
- 34 R. Y. Tang, M. Yuan, K. Liu, H. F. Li, J. T. Zhang and Y. Y. Tian, *J. Energy Inst.*, 2019, **92**, 1936–1943.
- 35 Q. Wu, *Fuel*, 2023, **332**, 126132.
- 36 W. Xie and H. Li, *J. Mol. Catal. A: Chem.*, 2006, **255**, 1–9.
- 37 C. Morterra and G. Magnacca, *Catal. Today*, 1996, **27**, 497–532.
- 38 J. Take, N. Kikuchi and Y. Yoneda, *J. Catal.*, 1971, **21**, 164–170.
- 39 A. Z. Khan and E. Ruckenstein, *J. Catal.*, 1993, **143**, 1–21.
- 40 E. S. Freeman, *J. Phys. Chem.*, 1956, **60**, 1487–1493.
- 41 B. D. Bond and P. Jacobs, *J. Chem. Soc. A*, 1966, 1265–1268.
- 42 K. H. Stern, *J. Phys. Chem. Ref. Data*, 1972, **1**, 747–772.
- 43 C. D. Wagner, *Faraday Discuss. Chem. Soc.*, 1975, **60**, 291–300.
- 44 A. Barrie and F. J. Street, *J. Electron Spectrosc. Relat. Phenom.*, 1975, **7**, 1–31.
- 45 J. Weitkamp, M. Hunger and U. Ryma, *Microporous Mesoporous Mater.*, 2001, **48**, 255–270.
- 46 K. Higuchi, M. Onaka and Y. Izumi, *Bull. Chem. Soc. Jpn.*, 1993, **66**, 2016–2032.
- 47 K. Tanabe, M. Misono, Y. Ono and H. Hattori, in *New Solid Acids and Bases*, Kodansha/Elsevier, Japan, 1989, ch. 2, p. 5.
- 48 H. Abimanyu, C. S. Kim, B. S. Ahn and K. S. Yoo, *Catal. Lett.*, 2007, **118**, 30–35.
- 49 Y. L. Wei, Y. M. Wang, J. H. Zhu and Z. Y. Wu, *Adv. Mater.*, 2003, **15**, 1943–1945.
- 50 L. Sun, X. Liu and H. Zhou, *Chem. Soc. Rev.*, 2015, **44**, 5092–5147.
- 51 H. Matsushashi and K. Arata, *J. Phys. Chem.*, 1995, **99**, 11178–11181.
- 52 J. H. Song, P. Chen, S. H. Kim, G. A. Somorjai, R. J. Gartside and F. M. Dautzenberg, *J. Mol. Catal. A: Chem.*, 2002, **184**, 197–202.
- 53 L. Meijia, W. Gang, Z. Zhongdong and T. Aizhen, *J. Fuel Chem. Technol.*, 2021, **49**, 104–112.
- 54 L. Fan, Y. Zhang, S. Liu, N. Zhou, P. Chen, Y. Liu, Y. Wang, P. Peng, Y. Cheng and M. Addy, *Energy Convers. Manage.*, 2017, **149**, 432–441.
- 55 J. Lai, Y. Meng, Y. Yan, E. Lester, T. Wu and C. H. Pang, *Korean J. Chem. Eng.*, 2021, **38**, 2235–2246.
- 56 O. S. Woo, N. Ayala and L. J. Broadbelt, *Catal. Today*, 2000, **55**, 161–171.
- 57 E. Giamello, A. Ferrero, S. Coluccia and A. Zecchina, *J. Phys. Chem.*, 1991, **95**, 9385–9391.
- 58 H. Matsushashi, M. Oikawa and K. Arata, *Langmuir*, 2000, **16**, 8201–8205.

